

Reaction Mechanism and Structural Evolution of Fluorographite Cathodes in Solid-State K/Na/Li Batteries

Zhengping Ding,* Chen Yang, Jian Zou, Shulin Chen, Ke Qu, Xiumei Ma, Jingmin Zhang, Jing Lu, Weifeng Wei, Peng Gao,* and Liping Wang*

Fluorographites (CF_x) are ultrahigh-energy-density cathode materials for alkali-metal primary batteries. However, they are generally not rechargeable. To elucidate the reaction mechanism of CF_x cathodes, in situ transmission electron microscopy characterizations and ab initio calculations are employed. It is found that it is a two-phase mechanism upon K/Na/Li ion insertion; crystalline KF (crystalline NaF nanoparticles and amorphous LiF) is generated uniformly within the amorphous carbon matrix, retaining an unchanged volume during the discharge process. The diffusivity for K/Na/Li ion migration within the CF_x is $\approx 2.2\text{--}2.5 \times 10^{-12}$, $3.4\text{--}5.3 \times 10^{-12}$, and $1.8\text{--}2.5 \times 10^{-11}$ cm² s⁻¹, respectively, which is comparable to the diffusivity of K/Na/Li ions in liquid-state cells. Encouraged by the in situ transmission electron microscopy (TEM) results, a new rechargeable all-solid-state Li/CF_x battery is further designed that shows a part of the reversible specific discharge capacity at the 2nd cycle. These findings demonstrate that a solid-state electrolyte provides a different reaction process compared with a conventional liquid electrolyte, and enables CF_x to be partly rechargeable in solid-state Li batteries.

volumetric energy density of 2595 Wh kg⁻¹ and 9313 Wh L⁻¹, respectively,^[2a] which can be used in Li primary cells.^[3] The theoretical energy density of CF_{1.0} cathode reaches 2595 Wh kg⁻¹,^[4] which is much higher than those cathodes of I₂ (591 Wh kg⁻¹), SOCl₂ (1470 Wh kg⁻¹), MnO₂ (1005 Wh kg⁻¹), Ag₂CrO₄ (515 Wh kg⁻¹), and CuS (1050 Wh kg⁻¹) in lithium metal batteries.^[5] CF_x also delivers a discharge specific capacity of 1061 mAh g⁻¹ (1439 Wh kg⁻¹) with a discharge plateau of 2.4 V^[6] in a Na/CF_x system, and 749 mAh g⁻¹ (1869 Wh kg⁻¹) with a discharge voltage plateau of 3.0 V in a K/CF_x system,^[7] which makes CF_x applicable for multiple alkali-ion batteries. Moreover, the irreversible conversion of CF_x into LiF and carbon during discharge, due to the high dissociation energy of LiF (6.1 eV), means the decomposition of LiF by charging alone is not possible.^[5,6b] Yazami et al. first demonstrated a reversible

While lithium ion batteries (LIBs) are widely applied in portable electronics and electric vehicles, cheaper, more advanced battery systems with higher energy and power densities, and improved safety performance remain in demand.^[1] Among the materials employed in cathode systems, conversion-type materials, such as halides, chalcogenides, and nitrides, demonstrate high specific capacities, offering lithium-metal batteries with high energy densities.^[1d,2] For example, fluorinated graphite (CF_x, $x = 1$) cathodes exhibit a high theoretical gravimetric energy density and

electrochemical reaction of CF_x with lithium in F ion batteries with a reversible capacity of ≈ 120 mAh g⁻¹.^[8] Later, Liu et al. reported a reversible Na/CF_x battery with a specific capacity of 786 mAh g⁻¹.^[6a] However, these batteries suffer from low conductivity, poor rate performance at low temperatures,^[9] initial voltage delay during the discharge process,^[3] and large heat generation at high discharge rates, which limit their application in harsh environments.^[5a,10] Therefore, a detailed study of the reaction mechanisms is urgently required for the further optimization.

Dr. Z.-P. Ding, S.-L. Chen, Dr. K. Qu, Dr. X.-M. Ma, Dr. J.-M. Zhang, Prof. P. Gao

International Center for Quantum Materials & Electron Microscopy Laboratory

School of Physics

Peking University

Beijing 100871, P. R. China

E-mail: zhengpingding@pku.edu.cn; p-gao@pku.edu.cn

C. Yang, Prof. J. Lu

State Key Laboratory for Artificial Microstructure

and Mesoscopic Physics

School of Physics

Peking University

Beijing 100871, P. R. China

J. Zou, Prof. L.-P. Wang

School of Materials and Energy

University of Electronic Science and Technology of China

Chengdu 611731, P. R. China

E-mail: lipingwang@uestc.edu.cn

Prof. W.-F. Wei

State Key Laboratory of Powder Metallurgy

Central South University

Changsha, Hunan 410083, P. R. China

Prof. P. Gao

Collaborative Innovation Center of Quantum Matter

Beijing 100871, P. R. China



The ORCID identification number(s) for the author(s) of this article can be found under <https://doi.org/10.1002/adma.202006118>.

DOI: 10.1002/adma.202006118

Various studies have been conducted to understand these battery systems using different techniques.^[3,10,11] For example, in situ X-ray diffraction (XRD) results suggested a simultaneous formation of a $\text{CF}_{(x-y)}\text{-Li}^+$ intermediate phase and crystal LiF ,^[9,11b] while other studies reported a formation of amorphous LiF followed by recrystallization to crystalline LiF .^[11a,c] The crystalline LiF is generated in an orientation that relates to the absorption energy of the solvents on the LiF surface.^[10] The reversibility and reaction mechanism of CF_x in Na/CF_x batteries were studied using soft X-ray absorption spectroscopy and nuclear magnetic resonance (NMR) techniques, which revealed reversible conversions between CF_x and NaF .^[6b] The liquid electrolyte was reported to act as an ion conductor and solution medium to dissolve and aggregate alkali fluoride crystals in a M-CF_x ($\text{M} = \text{Li}, \text{Na}, \text{and K}$) system, resulting in large crystalline alkali fluorides.^[7]

Despite intensive efforts focusing on the reaction mechanism, the structural evolution and reaction pathway of CF_x in $\text{K}/\text{Na}/\text{Li}$ batteries remain unclear. In this study, we use in situ transmission electron microscopy (TEM) with high spatial/temporal resolution to probe the phase transformation, intermediate phase, and volume change in real time (Figure 1a).^[12] We find that a two-phase reaction occurs during alkali-ion intercalation, and the diffusivity of $\text{K}/\text{Na}/\text{Li}$ ion intercalation in CF_x is $\approx 2.2\text{--}2.5 \times 10^{-12}$, $3.4\text{--}5.3 \times 10^{-12}$, and $1.8\text{--}2.5 \times 10^{-11} \text{ cm}^2 \text{ s}^{-1}$,

respectively. In situ electron diffraction patterns show the formation and even distribution of crystalline KF (or NaF nanoparticles or amorphous LiF) in the amorphous carbon matrix, leading to no volume change. Upon the insertion of K with a large ionic radius, the interlayer spacing of CF increases, while only subtle changes are observed during Na/Li ion insertion, both are confirmed through density functional theory (DFT) calculations. Our results show that reaction product growth is suppressed to form a homogeneous phase distribution of MF ($\text{M} = \text{K}, \text{Na}, \text{and Li}$) on the resulting carbon by the solid-state electrolytes, implying a possible reversible electrochemical reactivity of CF_x with lithium in a solid-state battery.

The bulk structure of the CF_x materials was characterized using XRD, TEM, selected-area electron diffraction (SAED), high-angle annular dark-field scanning TEM (HAADF-STEM) imaging, and energy-dispersive X-ray spectroscopy (EDS) mapping. As shown in Figure S1 in the Supporting Information, F atoms bond with C atoms in an sp^3 hybrid structure; the C atoms have a cyclohexane chair-type structure with AA stacking in the CF_x structure.^[7,13] Figure 1b shows a typical XRD pattern of the CF_x sample with broad diffraction peaks representing disordered phases. The peak at 13° is assigned to (002) reflection of the CF_x .^[5,14] The peak at 41° corresponds to (100) and (011) reflections; this is related to the C-C bond length and CF interlayer distance. Figure 1c shows a typical TEM bright-field

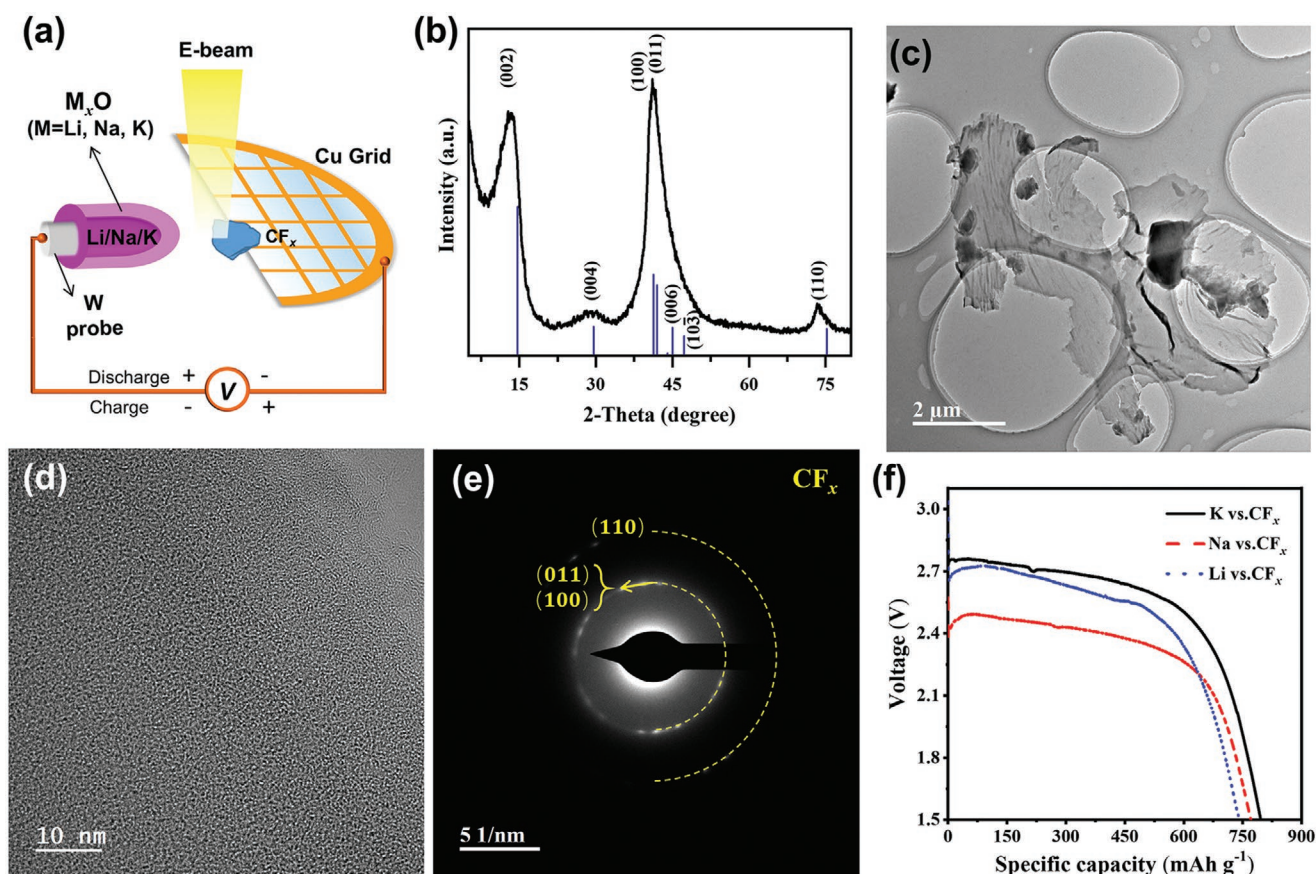


Figure 1. Structural characterizations and electrochemical performances of CF_x . a) Schematic illustration of the experimental setup for the in situ TEM experimental procedure. b) Powder XRD pattern of CF_x . c–f) TEM (c), HRTEM (d), and SAED (e) images of CF_x . f) Electrochemical measurements of CF_x in a K cell, Na cell, and Li cell in corresponding 1 M APF_6 ($\text{A} = \text{K}, \text{Na}, \text{Li}$) EC/DMC electrolyte.

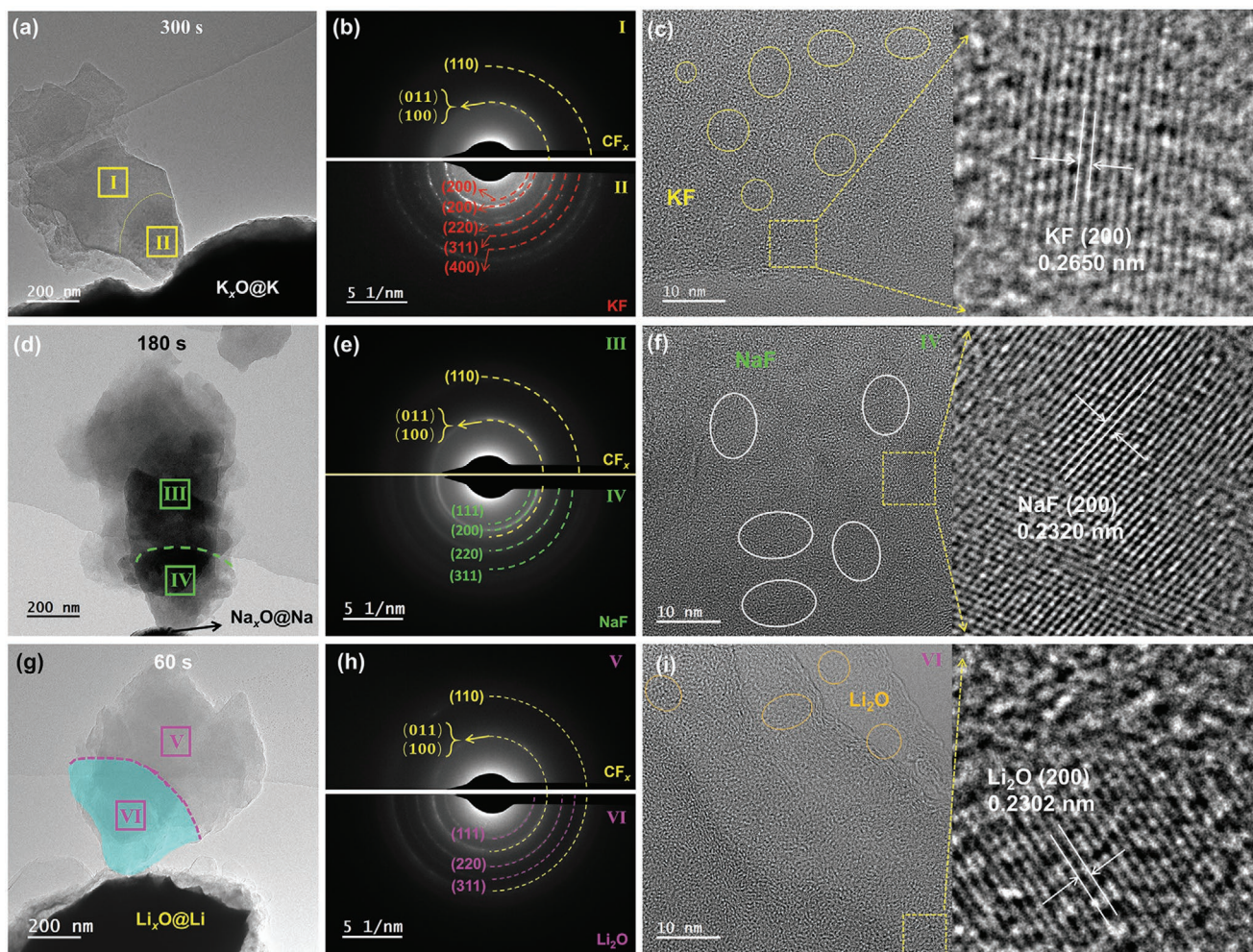


Figure 2. Characterization of CF_x following in situ ion insertion reaction. a) in situ TEM image of CF_x during potassiation at 300 s. b) SAED pattern obtained from pristine CF_x (I) and the reaction region (II). c) HRTEM images of region II. d) in situ TEM image of CF_x during sodiation at 180 s. e) SAED pattern obtained from pristine CF_x (III) and the reaction region (IV). f) HRTEM images of region IV. g) In situ TEM image of CF_x during lithiation at 60 s. h) SAED pattern obtained from pristine CF_x (V) and the reaction region (VI). i) HRTEM images of region VI.

image of the CF_x material with a large sheet-like topography, and the corresponding high-resolution TEM (HRTEM) image (Figure 1d) shows a disordered amorphous structure. As shown in Figure 1e, there are two diffraction rings representing the (100), (011), and (110) planes of CF_x in the SAED pattern, which is consistent with the XRD results. As shown in the HAADF-STEM image and corresponding color mixed EDS mapping of the CF_x sample (Figure S2, Supporting Information), C and F distributions are uniform in the sample.

Next, we tested CF_x ($x = 0.88$) as a cathode material for K-ion batteries (KIBs), Na-ion batteries (SIBs), and LIBs, and their typical discharge curves are shown in Figure 1f. Under the same CF_x discharge current, the discharge specific capacities of KIBs, SIBs, and LIBs are 796.1, 770.6, and 741.6 mAh g^{-1} , respectively, and the discharge plateaus are at ≈ 2.7 , ≈ 2.4 , and ≈ 2.6 V, respectively, which is in agreement with our previous work.^[7] As the ionic radius of K, Na, and Li is 138, 102, and 76 pm, respectively, the discharge specific capacity of Li-ion electrode materials under the same current density is supposed to be larger than that of Na- and K-ion materials because of the

higher mobility of Li^+ .^[15] However, the inverse phenomenon of this electrochemical performance is observed, when using CF_x as the cathode in KIBs, SIBs, and LIBs, probably due to the Stokes radius and electrolyte-assisted reaction mechanism.

The real time K/Na/Li ion insertion mobility and reaction mechanism of the CF_x cathode was studied using in situ all-solid-state nanobattery TEM technique (Figure 1a), which has been applied to study the reaction mechanism of electrode materials for batteries at high resolution.^[15b,16] In the in situ experiments, we used CF_x on a lacey carbon Cu TEM grid as the active cathode. Alkali metal (K/Na/Li) on a W tip is used as K/Na/Li source, and M_2O ($M = \text{K/Na/Li}$) layer is naturally formed on the fresh alkali metal when it is briefly exposed to the air. The native M_2O layer acts as solid electrolyte allowing $\text{K}^+/\text{Na}^+/\text{Li}^+$ transport and preventing electron transport. Many experiments have demonstrated that an M_2O layer is a good alkali-ion electrolyte, so charge/discharge experiments have been successfully conducted in many kinds of anode and cathode materials.^[12a,15b,17] **Figure 2**, **Figure 3**, Figures S3–S6, and Movies S1–S3 (Supporting Information) show the real

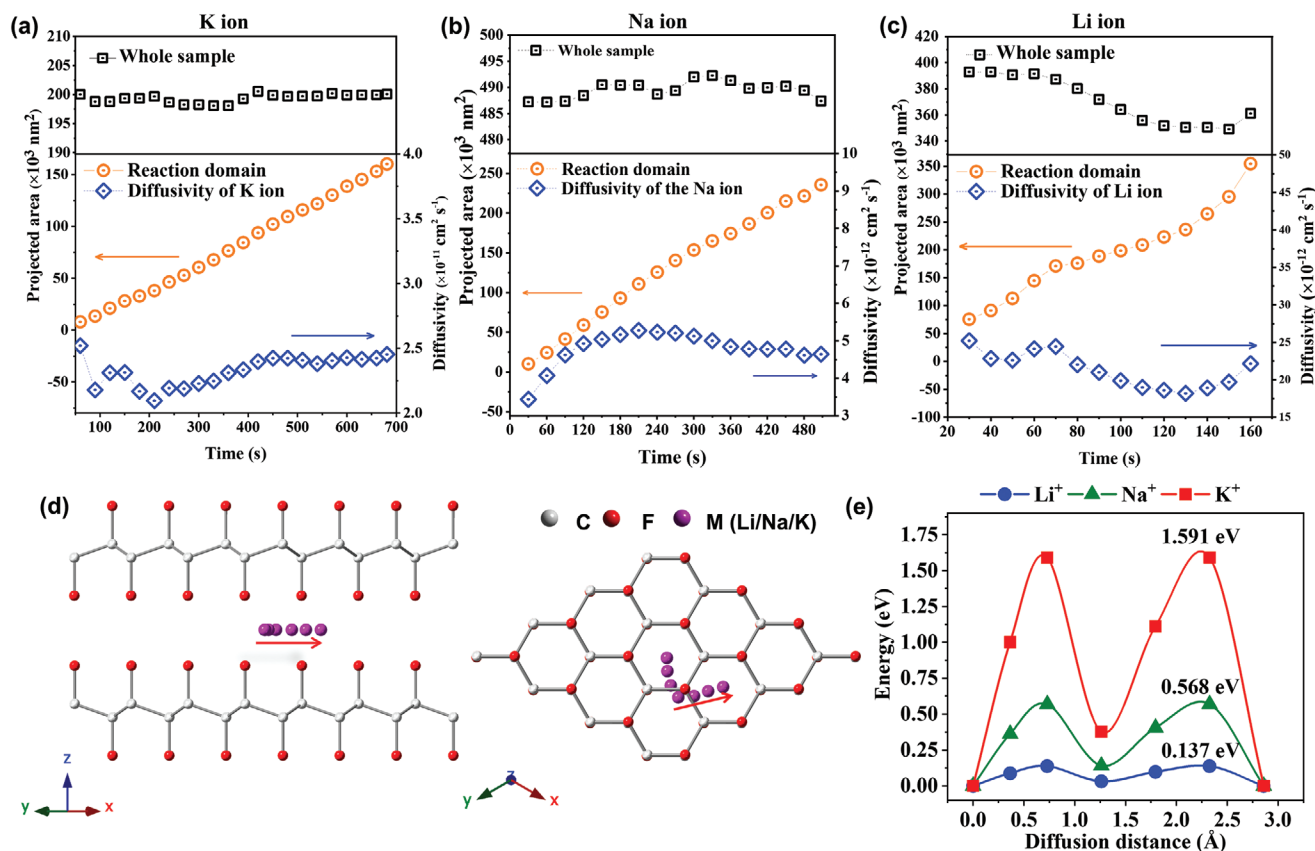


Figure 3. Ion migration kinetics of K/Na/Li ion insertion in CF_x . a–c) Projected area of the whole sample and reaction domain, and ion diffusivity are plotted as a function of reaction time during potassiation, sodiation, and lithiation. d) The diffusion pathway of K/Na/Li ions in CF_x . e) Energy profile of K/Na/Li ion diffusion.

time in situ time-series images and analysis results during K/Na/Li ion transport in a nano-sized CF_x sample. As shown in Figure S3a and Movie S1 in the Supporting Information, K uniformly intercalates into the CF_x during the discharge process and the projected area of the entire sample is almost unchanged, suggesting no volume change during the potassiation. Upon K intercalation, a clear phase boundary can be seen between pristine CF_x and the reacted domain in Figure S3a in the Supporting Information. The two-phase boundaries are more obvious in Figure S4 in the Supporting Information, which shows the STEM-EDS elemental mapping of C, F, and K. The two-phase reaction mode is further confirmed by electron diffraction patterns. As shown in Figure 2b, comparing the SAED pattern of the unreacted region (I) with that of region (II), additional rings arise due to the formation of KF. The SAED pattern after potassiation suggests that CF_x converted to KF and C. Figure 2c shows the HRTEM images of CF_x after potassiation. The C product maintains amorphous features, and KF nanoparticles (≈ 4 nm) are formed and uniformly distributed in the amorphous carbon matrix. Furthermore, considering the HAADF image contrast is roughly proportional to $Z^{1.7}$ (Z represents the atomic number), it is possible to confirm the two-phase boundary using a video taken with in situ HAADF-STEM imaging. Figure S7a–7d in the Supporting Information shows a series of real time HAADF-STEM images; the raw video is provided as Movie S4 in the Supporting Information.

As shown in Figure S7b in the Supporting Information, the brighter domain represents the reaction area with K ion intercalation, and the darker domain represents the pristine area. As shown in Movie S4 in the Supporting Information, movement of the phase boundary is observed during K ion insertion, and this clear phase boundary is characterized using EDS mapping (Figure S7e–7h, Supporting Information). Due to an increasing projected reaction area during the phase boundary motion, the K ion diffusivity in CF_x is estimated to be $2.2\text{--}2.5 \times 10^{-12} \text{ cm}^2 \text{ s}^{-1}$, in Figure 3a and Table S1 in the Supporting Information, based on the equation $D = d^2/t$, where D is ion diffusivity, d^2 is the projection area, and t is the diffusion time.^[18]

Sodiation of the CF_x sample exhibits a similar two-phase response, as shown in Figure 2d–f, and Figure S7i–7p and Movie S2 and S5 in the Supporting Information. Based on the TEM and HAADF-STEM images, we conclude that the volume of CF_x remains unchanged after sodiation (Figure 3b, and Figure S7i–7o, Supporting Information), and the SAED pattern (Figure 2e) shows a two-phase reaction representing the transformation of CF_x to NaF and C. After Na intercalation, 6–7 nm NaF nanoparticles are evenly distributed in the amorphous carbon matrix (Figure 2f). A two-phase boundary is observed in the elemental mapping of C, F, and Na (Figure S7m–7o, Supporting Information), and the Na ion diffusivity is $3.4\text{--}5.3 \times 10^{-12} \text{ cm}^2 \text{ s}^{-1}$, as calculated using the projected reaction area (Figure 3b and Movie S2 and Table S2 in the Supporting

Information). As a parallel comparison, the reaction of CF_x with Li^+ is also examined through in situ TEM, and the raw data are shown in Movie S3 in the Supporting Information. Upon Li ion intercalation, the projected area of CF_x remains the same and subsequently becomes smaller (because of sample rotational movement) (Figure 3c), indicating the volume remains unchanged. According to STEM-EDS mapping (Figure S6, Supporting Information), C and F remain uniformly distributed, suggesting no product aggregation. The two-phase boundary moves fast but is still clear (Figure 2g), and the Li ion diffusivity is $1.8\text{--}2.5 \times 10^{-11} \text{ cm}^2 \text{ s}^{-1}$, as calculated using the projected reaction area (Figure 3c and Table S3, Supporting Information). As shown in Figure S6e–6f in the Supporting Information, the electron energy loss spectroscopy (EELS) Li K edge and F K edge spectra are in agreement with that reported for LiF,^[19] suggesting that LiF is formed after Li ion intercalation. However, in the SAED pattern of pristine CF_x (region V) and after lithiation (region VI) (Figure 2h), the rings of region VI could be assigned to (111), (220), and (311) planes of Li_2O , indicating that Li_2O is formed after lithiation. As shown in Figure 2i, Li_2O nanoparticles with a size of $\approx 3 \text{ nm}$ are uniformly distributed in the amorphous carbon matrix after lithiation. According to previous work, LiF crystals have been formed and detected using XRD analysis and NMR spectra in liquid Li ion primary batteries during discharge process.^[3,5a,7,10,11] Considering it is an all-solid-state environment in the in situ TEM experiment, amorphous LiF is formed in the Li– CF_x system, which is consistent with that reported by Rangasamy.^[20] As for the formed Li_2O , Li will diffuse along the surface of the materials, and the active Li will react with trace O_2 in the TEM chamber, resulting in Li_2O formation in CF_x .

Upon formation of a solid-state M– CF_x in the in situ TEM system, all alkali ions uniformly diffuse across the materials, with diffusivities of $2.2\text{--}2.5 \times 10^{-12} \text{ cm}^2 \text{ s}^{-1}$, $3.4\text{--}5.3 \times 10^{-12} \text{ cm}^2 \text{ s}^{-1}$, and $1.8\text{--}2.5 \times 10^{-11} \text{ cm}^2 \text{ s}^{-1}$ for K, Na, and Li ion insertion in CF_x , respectively. However, in the liquid electrolyte, the discharge specific capacities of CF_x for KIBs, SIBs, and LIBs are 796.1 mAh g^{-1} , 770.6 mAh g^{-1} , and 741.6 mAh g^{-1} , respectively, indicating that the ion mobility of K is higher than that of Na and Li. In the liquid-state M– CF_x system, large fluoride crystals are formed and a higher K^+ apparent diffusivity than Na^+ and Li^+ is observed ($10^{-14}\text{--}10^{-10} \text{ cm}^2 \text{ s}^{-1}$ for K^+/Na^+ diffusion and $10^{-15}\text{--}10^{-11} \text{ cm}^2 \text{ s}^{-1}$ for Li^+ diffusion).^[7] However, if organic solvent molecules are absent from a solid-state battery system, the ion diffusivity is determined by alkali-ion insertion ability, as demonstrated by the high ion diffusivities observed for the Li ion in our study using in situ TEM.

To further understand the alkali-ion intercalation behavior in CF_x , DFT is applied to calculate the structure and physical-chemical properties after K/Na/Li-ion intercalation (Figures S8 and S9, Supporting Information). The partial density of states (PDOS) of pristine CF and K/Na/Li adsorbed CF ($\text{M}_2\text{C}_4\text{F}_4$) are acquired through DFT calculations and shown in Figure S8 in the Supporting Information. Herein, and based on the theoretical calculations, the CF structure is a semiconductor with a bandgap of 2.4 eV, which is consistent with the previous work.^[21] For a successful application as battery cathodes, good electrical conductivity is important. After adsorption of K/Na/Li in CF, the Fermi level contains various electronic states, indicating the improved electric conductivity. As shown in Figure 1f,

the initial discharge plateau is low, and then increases to the original state as the discharge process progresses, this is related to the increased conductivity resulting from K/Na/Li adsorption. Furthermore, the ion diffusion pathways and energy profiles for the diffusion of K/Na/Li ions in CF are also calculated and shown in Figure 3d,e. Diffusion of K/Na/Li ions at the interlayer of CF proceeds via a zigzag pathway (Figure 3d); the energy diffusion barrier for K/Na/Li ions is 1.591 eV, 0.568 eV, and 0.137 eV, respectively (Figure 3e). A low energy diffusion barrier indicates a high ionic mobility, which is consistent with our experimental results (i.e., $2.2\text{--}2.5 \times 10^{-12} \text{ cm}^2 \text{ s}^{-1}$ for K, $3.4\text{--}5.3 \times 10^{-12} \text{ cm}^2 \text{ s}^{-1}$ for Na, and $1.8\text{--}2.5 \times 10^{-11} \text{ cm}^2 \text{ s}^{-1}$ for Li). By comparison, in a solid-state battery, ion diffusion is determined by the ion diffusion barrier in bulk structure. While in a liquid-state battery, the ion diffusion is affected by organic solvent simultaneously, resulting in reverse phenomena in liquid electrolyte batteries.

As discussed above, different alkali ions result in an unchanged volume during the solid-state reaction; alkali fluoride nanoparticles evenly distributed in the carbon matrix are the resultant products. To probe the phase evolution of CF_x during alkali-ion insertion, in situ electron diffraction is applied to study the samples during the entire discharge process and the results are shown in Figure 4, and Figure S10 and Movie S6–S8 in the Supporting Information. Figure 4a presents the radial intensity profiles as a function of reaction time retrieved from in situ SAED (Movie S6, Supporting Information) upon K ion intercalation. The original radial intensity profiles are acquired by integrating the intensity of a series of SAED patterns along the r direction over the full 2π range, and the final radial intensity profiles are obtained after background subtraction using the power-law model (Figure 4a). Before potassiation, characteristic diffraction rings for CF_x corresponding to (100), (011), and (110) peaks are observed (Figure S10a, Supporting Information). As K ion intercalation progresses, several new diffraction rings appear, initially faint, then become stronger with time. In the corresponding radial intensity profiles (Figure 4a), new diffraction peaks that become stronger with time and these new diffraction peaks are assigned to the (200) and (220) planes of KF. As shown in Figure 4b, the diffraction peaks for pristine CF_x remain and shift left over lower distances, indicating the spacing of monolayer CF increased and the C–C bond length increased after K ion intercalation. Moreover, Figure 4c shows the full width at half maxima (FWHM) for the KF (200) peak, and the corresponding calculated crystal size of KF-based on the Scherrer equation.^[22] After potassiation, $\approx 3.3 \text{ nm}$ KF nanoparticles are immediately formed, and the particle sizes remain the same with increasing reaction time, which is in agreement with HRTEM results. The formation of KF nanoparticles also demonstrates the migration of F ions during the reaction, implying a conversion reaction occurs during potassiation. As a parallel comparison, the reaction of CF_x with Na ions is examined with in situ electron diffraction, the raw data from a typical experiment are shown in Movie S7 in the Supporting Information. The radial intensity profile and corresponding diffraction patterns with false colors are shown in Figure 4d–f and Figure S10b in the Supporting Information. As the Na ion intercalation progresses (Figure 4d), several new diffraction rings which could be indexed to the cubic

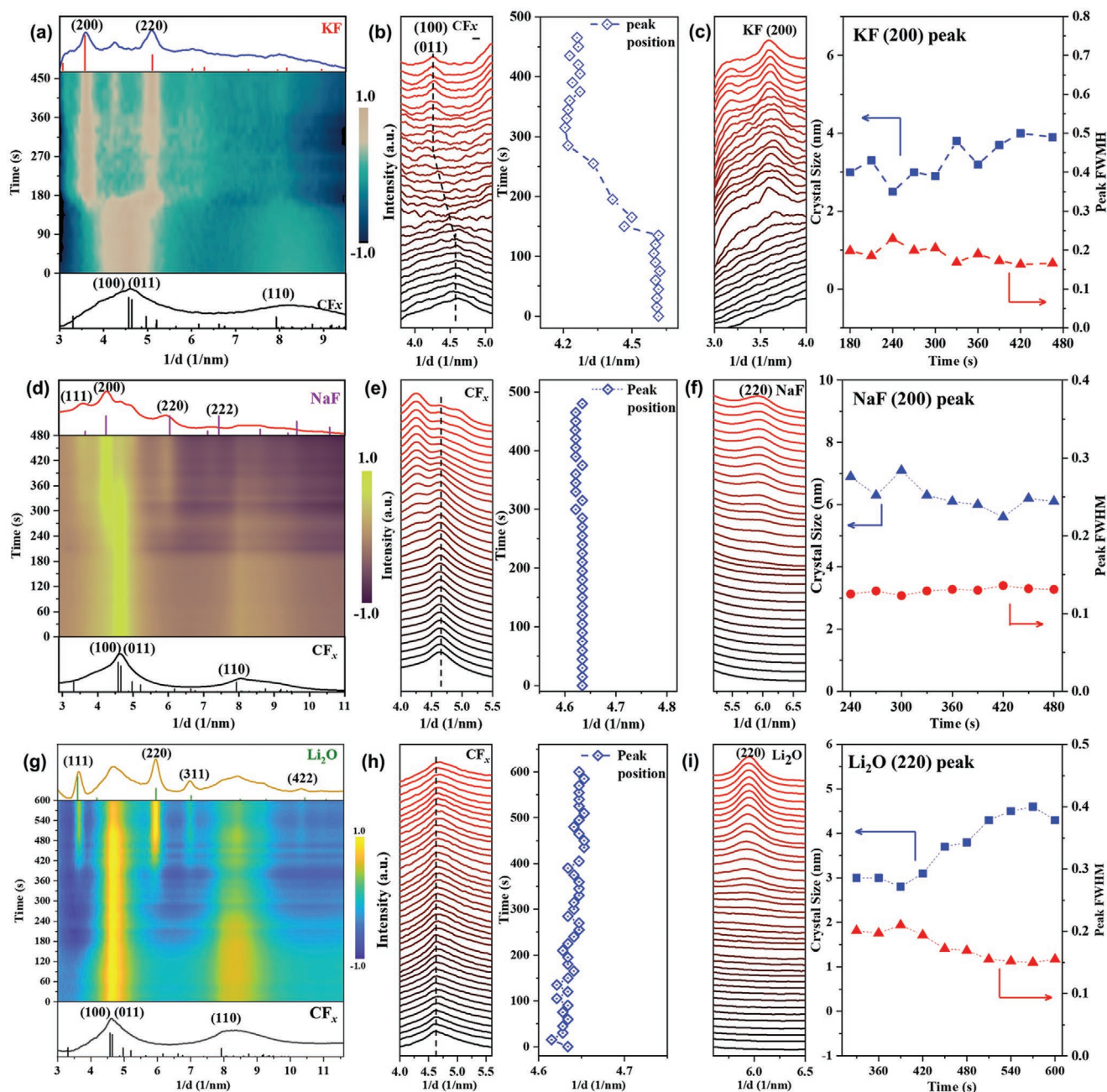


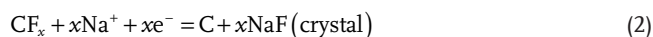
Figure 4. Phase evolution tracking using in situ SAED of CF_x . a) In situ SAED intensity profile and b) peak position of CF_x as a function of reaction time during potassiation. c) Full width at half maxima (FWHM) for the KF peak (200), and the corresponding calculated crystal size of KF-based on the Scherrer equation. d) In situ SAED intensity profile and e) peak position of CF_x as a function of reaction time during sodiation. f) FWHM for the NaF peak (200), and the crystal size of NaF. g) In situ SAED intensity profile and h) peak position of CF_x as a function of reaction time during lithiation. i) FWHM for the Li_2O peak (220), and the crystal size of Li_2O .

NaF (space group $Fm-3m$), appear, faint initially and become stronger with time. As shown in Figure 4e, different to K ion insertion, the CF_x diffraction peak does not shift during Na ion intercalation, suggesting the spacing of the carbon monolayer product is unchanged. As shown in Figure 4f, ≈ 6.3 nm NaF nanoparticles are formed based on the (200) peak of NaF; their size is retained with increasing reaction time. The lithiation of CF_x exhibits a similar phase evolution phenomenon, and is shown in Figure 4g–i and Movie S8 and Figure S10c in the

Supporting Information. Upon Li ion intercalation, several new diffraction rings appear, initially faint, and become stronger over time (Figure S10c, Supporting Information). As shown in Figure 4g, as the reaction time increases, new, higher, diffraction peaks appear; these new peaks can all be indexed to the cubic Li_2O phase (space group $Fm-3m$). Furthermore, the (100), (011), and (110) peak position for the resulting carbon monolayer maintain with increasing reaction time (Figure 4h), implying that the amorphous feature of CF_x remains unaltered

after lithiation. As shown in Figure 4i, the Li₂O nanoparticle size slowly increases from 3 nm to 5 nm, which may account for Li aggregation on the surface. As we know, if amorphous LiF is formed in a solid-state Li–CF_x system, no LiF crystal diffraction rings are detected during in situ electron diffraction. During K/Na/Li intercalation, the original diffraction peaks for the (100) and (011) planes change; this is connected to the embedded ion structure. Figure S9a in the Supporting Information shows the optimized structure of M₂C₄F₄ which is calculated using DFT. As shown in Figure S9a in the Supporting Information, the distance of the CF monolayer for pristine C₄F₄ is 5.574 Å, and becomes 7.285 Å, 6.592 Å, and 6.288 Å after K/Na/Li ion insertion, respectively. The corresponding diffraction profile is calculated using CrystalDiffract software based on the optimized structure and is shown in Figure S9b in the Supporting Information. The peak position for the (100) and (011) plane shifts to the right with increased distance after K ion insertion, while the peak position remains unchanged for Na ion insertion, which is consistent with experimental results. Remarkably, the peak position shifts left due to the transformation from chair configuration to a flat graphite-like structure during Li intercalation, which is in accordance with the in situ experiments and as reported in previous studies.^[7,23]

As mentioned above, the electrochemical solid-state reaction of CF_x with alkali metal ions is expected to behave according to the following equations:



These reactions are different from liquid-state batteries. In liquid-state batteries, the alkali fluoride will dissolve and then aggregate on the CF_x surface, resulting in large crystals (≈200–300 nm) and theoretical volume expansion of the electrode based on bulk phase structure (56.9% for K insertion, 32.9% for Na insertion, and 22.9% for Li insertion).^[3,6a,7] However, in the solid-state system, alkali fluoride nanoparticles are formed immediately and the size of the alkali fluoride nanoparticles remains unchanged with time. As the alkali fluoride nanoparticles are uniformly distributed in the amorphous carbon matrix and the size remains unchanged during the reaction, volume expansion does not occur, which is beneficial for solid-state battery systems. Moreover, as for lithium-ion batteries, large crystal LiF nanoparticles are formed in a liquid-state battery,^[7] while amorphous LiF is formed in solid-state batteries. Furthermore, the diffusivity in solid-state CF_x cell is 2.2–2.5 × 10^{−12} cm² s^{−1}, 3.4–5.3 × 10^{−12} cm² s^{−1}, and 1.8–2.5 × 10^{−11} cm² s^{−1} for K, Na, and Li ion insertion, respectively, which is comparable to the diffusivity of K/Na/Li ions in liquid-state alkaline cells (10^{−14}–10^{−10} cm² s^{−1} for K⁺/Na⁺ diffusion and 10^{−15}–10^{−11} cm² s^{−1} for Li⁺ diffusion),^[7] this also indicates that CF_x is a suitable cathode for solid-state cells.

CF_x is known to have a large high theoretical energy density (2595 Wh kg^{−1} when x = 1).^[4] It is widely accepted that the reaction of CF_x with lithium is likely irreversible ascribed to the high dissociation energy of LiF (6.1 eV), meaning Li/CF_x can only be used as a primary cell. However, metal fluorides (MF_x, M = Fe,

Cu, Co, Mn...) have been proved to own high capacities due to the reversible conversion reaction of LiF and transition metal.^[24] During the charge/discharge process of metal fluoride, LiF can be formed/decomposed in the potential range of 1.2 to 4.5 V.^[24d] The irreversible capacity of metal fluoride increases due to the aggregation and continuous coarsening of transition metal nanoparticles during repeated conversion reaction cycles.^[24a,25] In Li/CF_x liquid-state batteries, the large LiF crystals (≈200–300 nm) are formed and aggregate on the CF_x surface,^[10] leading to phase separation of LiF and the resulted carbon. In a word, the irreversibility of CF_x with Li in liquid-state battery mainly come from phase separation of LiF and the resulted carbon, instead of electrochemically indecomposable of LiF.

As discussed above in the in situ TEM results, phase separation and product growth can be suppressed by a solid-state electrolyte, where amorphous LiF is produced and distributed uniformly in the resulting carbon matrix in the in situ solid-state nanocell. Hence, the reaction of CF_x with lithium is likely reversible in all-solid-state battery. To verify this idea, the CF_x|LiPF₆-EC/DMC|Li liquid-state and CF_x|LiTFSI-PEO|Li solid-state battery are fabricated, and their electrochemical performances are tested and shown in Figure 5 and Table S4 in the Supporting Information. As shown in Figure 5a and Table S4 in the Supporting Information, the 1st discharge specific capacity of the liquid-state battery is 737.3 mAh g^{−1}, and the following charge capacity is 51.8 mAh g^{−1} when the voltage is up to 4.5 V, reflecting the irreversibility of CF_x|LiPF₆-EC/DMC|Li liquid-state battery. As a comparison, the 1st discharge specific capacity of CF_x|LiTFSI-PEO|Li solid-state battery is 512.2 mAh g^{−1}, which is comparable to the liquid-state battery (Figure 5b). During charging, the charge potential raises up to 3.6 V quickly, then increases slowly to 4.5 V with a charge specific capacity of 197.5 mAh g^{−1}, and the following discharge capacity is 160.7 mAh g^{−1}. There are two slope plateaus at about ≈2.7 V and ≈2.0 V in the 2nd discharge profile, indicating that solid-state Li–CF_x batteries is partially reversible in the charge/discharge process. To verify the rechargeability of CF_x, Super-P|LiTFSI-PEO|Li solid-state battery is also fabricated by substitution of CF_{0.88} with super P conductive carbon. The charge-discharge profile is shown in Figure 5c, and the 2nd discharge specific capacity is only 10.6 mAh g^{−1}. Moreover, cyclic voltammogram (CV) curves of Super-P|LiTFSI-PEO|Li and CF_x|LiTFSI-PEO|Li battery are tested and shown in Figure 5d and Figure S11 in the Supporting Information. As shown in Figure 5d, there is a characteristic cathodic peak at 2.10 V in the first negative scanning to 1.50 V, and it shifts to 2.20 V at the second and third discharging process, referring to the reduction conversion reaction from CF_x to LiF and C. During the positive scan, an anodic peak at 4.36 V is observed, corresponding to the oxidation reaction. However, no apparent cathodic and anodic peak are observed in the CV curves of Super P (Figure S11, Supporting Information). Therefore, in the window from 1.5–4.5 V, the LiTFSI-PEO electrolyte is stable, indicating that the charge capacity is attributed to decomposing LiF and CF_x is rechargeable in a solid-state battery. As shown in Figure 5e,f, when the electrochemical window is expanded to 0.5–4.5 V, the discharge capacity and charge capacity increase to 896.3 and 537.8 mAh g^{−1}, respectively. In subsequent cycles, the discharge capacities decrease gradually, and the discharge capacity is 543.3, 320.5

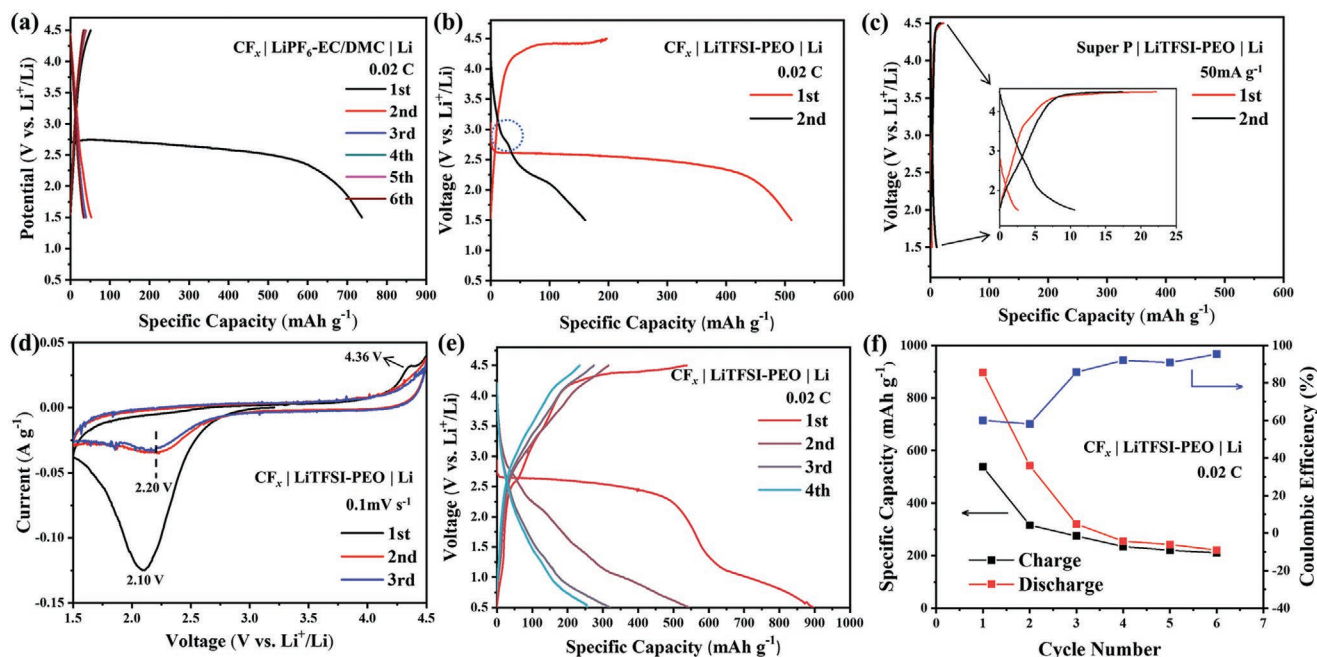
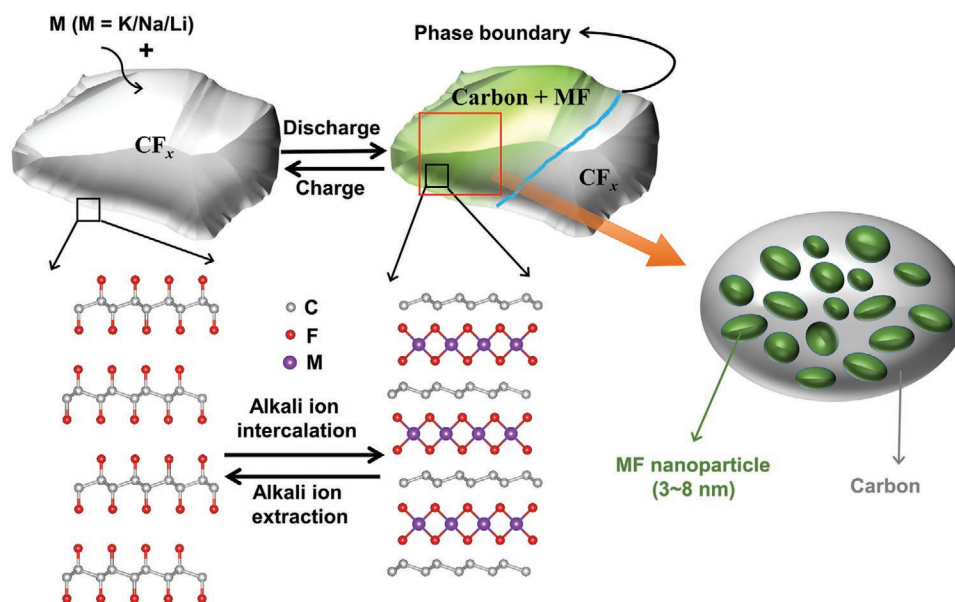


Figure 5. Electrochemical performance of fluorinated graphite as the cathode in liquid-state and solid-state Li-ion battery. a) Charge–discharge voltage profiles of $\text{CF}_x|\text{LiPF}_6\text{-EC/DMC}|\text{Li}$ liquid-state battery at 0.02 C in the voltage range from 1.5 to 4.5 V. b) Charge–discharge voltage profiles of $\text{CF}_x|\text{LiTFSI-PEO}|\text{Li}$ solid-state battery at 0.02 C in the voltage range from 1.5 to 4.5 V. c) Charge–discharge voltage profiles of Super P|LiTFSI-PEO|Li solid-state battery at 50 mA g^{-1} in the voltage range from 1.5 to 4.5 V. d) Cyclic voltammograms curves of $\text{CF}_x|\text{LiTFSI-PEO}|\text{Li}$ solid-state battery. e) Charge–discharge voltage profiles of $\text{CF}_x|\text{LiTFSI-PEO}|\text{Li}$ battery at 0.02 C in the voltage range from 0.5 to 4.5 V. f) Cycling performance of $\text{CF}_x|\text{LiTFSI-PEO}|\text{Li}$ solid-state battery at 0.02 C in the voltage range from 0.5 to 4.5 V.

and 221.0 mAh g^{-1} at the 2nd, 3rd, and 6th cycle, respectively (Table S4, Supporting Information). However, it can be seen that the gap between charge and discharge potential is about 2 V, which is too high and will lower the energy efficiency, and the cycle stability for solid-state Li- CF_x battery is poor. More efforts should be applied to improve the electrochemical performances of all-solid-state Li- CF_x battery.

As discussed above, the in situ all-solid-state nanobattery TEM technique is employed to explore the reaction mechanism of CF_x with K/Na/Li during ion intercalation/extraction. In the M/ CF_x liquid-state battery, the apparent K ion diffusivity is higher than that of Li and Na ions, and the discharge products are amorphous carbon and large alkali fluoride crystals. In the solid-state battery system, the alkali-ion intercalation reaction



Scheme 1. Reaction mechanism schematic of CF_x and alkali ions (K/Na/Li) during the discharge process in an in situ TEM all-solid-state cell.

mechanism is significantly different from that of the liquid-state system, see **Scheme 1**. In the M/CF_x solid-state battery system, a two-phase reaction and phase boundary movement (Figure 2,3) are observed during alkali-ion intercalation. Based on the two-phase boundary movement (Figure 3), the diffusivity of K/Na/Li ion intercalation in CF_x is $2.2\text{--}2.5 \times 10^{-12} \text{ cm}^2 \text{ s}^{-1}$, $3.4\text{--}5.3 \times 10^{-12} \text{ cm}^2 \text{ s}^{-1}$, and $1.8\text{--}2.5 \times 10^{-11} \text{ cm}^2 \text{ s}^{-1}$, respectively, which is further investigated through DFT calculations. According to the in situ electron diffraction results (Figure 4), crystalline KF, NaF nanoparticles, and amorphous LiF are formed and remain unchanged with increasing reaction time; furthermore, these alkali fluoride nanoparticles are uniformly distributed in the amorphous carbon matrix (Scheme 1), resulting in no volume change. According to the volume expansion limit and high ion diffusivity, the $CF_{0.88}$ possess a discharge capacity of 512.2 mAh g^{-1} in all-solid-state $CF_x|PEO\text{-}LiTFSI|Li$ cell in the voltage window of $1.5\text{--}4.5 \text{ V}$ (Figure 5b). Moreover, the in situ TEM results reveal solid-state electrolytes have multi-functions, especially on suppressing the discharge product growth and result in a homogeneous phase distribution, which makes the CF_x have the potential to be rechargeable as second ion battery.

In summary, we reveal the reaction mechanism and phase evolution of CF_x with K/Na/Li during ion intercalation using in situ TEM. During alkali-ion insertion, a two-phase reaction and clear two-phase boundary are observed, and the diffusivity of K/Na/Li ion insertion in CF_x is calculated to be $2.2\text{--}2.5 \times 10^{-12} \text{ cm}^2 \text{ s}^{-1}$, $3.4\text{--}5.3 \times 10^{-12} \text{ cm}^2 \text{ s}^{-1}$, and $1.8\text{--}2.5 \times 10^{-11} \text{ cm}^2 \text{ s}^{-1}$, respectively, based on movement of the phase boundary. Nano-sized crystalline KF/NaF particles and amorphous LiF are formed and evenly distributed in the amorphous carbon matrix. Upon the insertion of K ions, which have a large ionic radius, the spacing distance of the CF monolayer increases, and this is confirmed by DFT calculations. As the alkali fluoride nanoparticles are uniformly distributed in the amorphous carbon matrix and the size remains unchanged during the reaction, volume expansion for CF_x is relieved and does not occur. CF_x cathode demonstrates a potential reversible behavior in LiTFSI-PEO solid-state electrolyte. Our findings provide a fundamental understanding of the electrochemical processes and phase transitions of CF_x cathodes and valuable insights for the development of high-performance alkaline batteries in solid-state electrolytes.

Experimental Section

Electrochemical Characterization: Fluorinated graphite $CF_{0.88}$ was purchased from Hubei Zhuoxi Fluorochemical Co., LTD, China and used without further purification. Powder X-ray diffraction patterns were obtained using a Bruker AXS D8 Advance X-ray diffractometer (Germany) with Cu $K\alpha$ radiation in a step size of 0.02° at a dwell time of 1 s. The conductivity of CF_x is relatively low.^[3,5a,26] To improve the conductivity of the electrode, the $CF_{0.88}$ materials were mixed with conductive acetylene black and poly(vinylidene fluoride) binder at a weight ratio of 7:2:1 and then dissolved completely in *N*-methyl-2-pyrrolidone. After stirring for 1 h, the obtained slurry was homogeneously pasted onto Al foil and dried at 110°C for 12 h in a vacuum oven. The coated foil was cut into circular pieces with a diameter of 12 mm. The mass loading for active materials ($CF_{0.88}$) was around 2 mg cm^{-2} . A cathode electrode, a separator (glass fiber), and a metallic anode (K, Na, Li) were assembled

into a coin-type half-cell (CR 2032) in an Ar-filled glove box (MBraun, Germany). The electrolyte solution was prepared by dissolving 1 M APF_6 ($A = K, Na, Li$) in ethylene carbonate/dimethyl carbonate (1:1, v/v). The discharge tests were performed using a LANHE CT2001A cell test system at room temperature from 1.5 V/0.5 V to 4.5 V at a constant current rate of $0.02C$ ($1C = 821 \text{ mA g}^{-1}$).

For the solid-state Li cell, the separator film and electrolyte were replaced with LiTFSI-PEO-based solid-state electrolyte. As for the preparation of the LiTFSI-PEO solid-state electrolyte, the molar ratio of EO (Ethylene Oxide): Li was fixed at 20:1, and Al_2O_3 (4 wt% of LiTFSI-PEO) was applied as the filler. Typically, 12.36 mg nano Al_2O_3 (20 nm, Aladdin Reagent Co., LTD.) was dispersed in 10 mL acetonitrile to make a suspension. Then, 233 mg PEO ($M_v \approx 600\,000$, Aladdin Reagent Co., LTD.) and 76 mg LiTFSI were added into the suspension. A homogenous solution can be acquired after continuous stirring for four hours. Afterwards, 1 mL LiTFSI-PEO solution dried on a PTFE plate template ($\varphi = 19 \text{ mm}$) to obtain the film. As for the PEO-based cathode electrodes, the weight proportion of $CF_{0.88}$, super P, and LiTFSI-PEO was adjusting to 6:2:2. LiTFSI-PEO was used as both a binder and a solid-state electrolyte. The coating process was similar to that of $CF_{0.88}$ /super P/PVDF electrodes via using acetonitrile solution. The mass loading of $CF_{0.88}$ is about 1.5 mg cm^{-2} . For a comparison, bare super P electrode was prepared by substitution of $CF_{0.88}$ with super P. After assembling, the coin cells were sealed with a pressure of 50 kg cm^{-2} . The electrochemical tests are at 60°C for solid-state cells and at room temperature for liquid-state cells.

In Situ TEM: In situ TEM, HAADF, and SAED were carried out using a Tecnai F20 at 200 kV equipped with an Oneview IS (Gatan) camera. Figure 1a shows a schematic illustration of the in situ TEM experimental procedure. The in situ TEM electrochemical cell was incorporated into an electrical TEM specimen holder (PicoFemto, China), where $CF_{0.88}$ was dispersed on a TEM half Cu-grid with a lacey carbon support acting as the active electrode material, current collector, and conductive carbon; alkali metal (Li/Na/K) was coated on an electrochemically etched sharp tungsten probe and acted as the counter electrode. During the transfer process, the active alkali metal probe was intentionally exposed to the air (less than 10 s) to form a M_xO ($M = Li, Na, \text{ and } K$) layer on the alkali metal surface, the formed M_xO acted as a solid-state electrolyte. To eliminate the radiation damage on the materials, the electron dose rate was adjusted to be less than $10 \text{ e } \text{Å}^{-2} \text{ s}^{-1}$ during the in situ imaging processes. The control-experiments were conducted under the same conditions, and the results were exhibited in Movie S9–S11 in the Supporting Information. As shown in Figure S12 in the Supporting Information, CF_x is very stable under electron beam irradiation, while a small quantity of electron beam damage of M_xO ($M = K, Na, \text{ and } Li$) solid electrolyte and M anode are observed after 1200 s electron beam irradiation. Thus, the all-solid-state nanobattery is stable during the whole in situ experiments. A constant negative potential (-3 V) was applied between $CF_{0.88}$ and the K/Na/Li source during the discharge process after CF_x is contacted with M_xO electrolyte.

The high-resolution TEM images, dark-field images, and EDS mapping were acquired using a FEI Tecnai F20 with an Oxford X-Max^N TSR EDS detector. Electron energy loss spectroscopy (EELS) was conducted on an aberration-corrected FEI (Titan Cubed Themis G2) equipped with an X-FEG gun operated at 300 kV with $\approx 50 \text{ pA}$ beam current. The EELS data was collected using a Gatan Enfium system with a collection semi-angle of 5.9 mrad , a convergence semi-angle of 25 mrad and a dispersion of 0.25 eV/ch . The data was processed using DigitalMicrograph (Gatan) software.

First-Principles Calculations: The pristine AA-stacking CF structure was used based on our previous work.^[7] The Vienna ab initio simulation package (VASP) was used to optimize the structure and perform electronic state calculations.^[27] The “energy” code in the Cambridge Sequential Total Energy Package (CASTEP) was performed to obtain the precise energies of the materials.^[28] These calculations were based on density functional theory (DFT), and generalized gradient approximation (GGA) combined with the adoption of the Perdew–Burke–Ernzerhof

(PBE) form.^[29] The Monkhorst–Pack scheme sampling method with a separation of 0.02 Å⁻¹ was used to generate the k-points mesh. The convergence thresholds were set as 10⁻⁶ eV for energy and 10⁻³ eV Å⁻¹ for force.

The climbing image nudged elastic band (CI-NEB) method implemented in the VASP transition state tools was used to calculate the K/Na/Li atom diffusion barriers.^[30] Herein, one K/Na/Li atom was initially adsorbed in the hollow site of the 3 × 3 × 1 CF supercell (including 36 C and 36 F atoms), based on previous work.^[23] Next, the K/Na/Li atom diffused to the adjacent hollow site with the fixed lattice constant *c* (perpendicular to the layer plane) of 12.28 Å (the lattice constant of CF^[7,23]). Such a supercell was large enough to avoid interactions between K/Na/Li atoms in different supercells and was used to simulate initial diffusion K/Na/Li at low concentrations.^[31]

Supporting Information

Supporting Information is available from the Wiley Online Library or from the author.

Acknowledgements

Z.-P.D. and C.Y. contributed equally to this work. This work was supported by the National Key R&D Program of China (2016YFA0300903, 2016YFA0300804, 2016YFB0700600, and 2017YFA206303), National Natural Science Foundation of China (51672007, 11974023, 52072061, and 91964101), the Key R&D Program of Guangdong Province (2018B030327001, 2018B010109009), the China Postdoctoral Science Foundation (2019M650333), and the International Science and Technology Cooperation Program of China (2014DFE00200). L.-P.W. thanks the Fundamental Research Funds for the Central Universities, China (ZYGX2019Z008). P.G. gratefully acknowledges the support from “2011 Program” Peking-Tsinghua-IOP Collaborative Innovation Center of Quantum Matter. The authors acknowledge the Electron Microscopy Laboratory at Peking University for the use electron microscopes. This project was also partly supported by the State Key Laboratory of Powder Metallurgy, Central South University, Changsha, China. The authors also thank the High-performance Computing Platform of Peking University.

Conflict of Interest

The authors declare no conflict of interest.

Keywords

alkali diffusivity, alkali-ion batteries, fluorinated graphite

Received: September 7, 2020

Revised: October 25, 2020

Published online: December 9, 2020

- [1] a) M. Armand, J. M. Tarascon, *Nature* **2008**, 451, 652; b) B. Kang, G. Ceder, *Nature* **2009**, 458, 190; c) J. M. Tarascon, M. Armand, *Nature* **2001**, 414, 359; d) K. Turcheniuk, D. Bondarev, V. Singhal, G. Yushin, *Nature* **2018**, 559, 467; e) G. Assat, J. M. Tarascon, *Nat. Energy* **2018**, 3, 373.
- [2] a) L. P. Wang, Z. R. Wu, J. Zou, P. Gao, X. B. Niu, H. Li, L. Q. Chen, *Joule* **2019**, 3, 2086; b) S. H. Yu, X. Feng, N. Zhang, J. Seok, H. D. Abruna, *Acc. Chem. Res.* **2018**, 51, 273.
- [3] Y. Ahmad, M. Dubois, K. Guérin, A. Hamwi, W. Zhang, *Carbon* **2015**, 94, 1061.
- [4] D. C. Bock, A. C. Marschilok, K. J. Takeuchi, E. S. Takeuchi, *Electrochim. Acta* **2012**, 84.
- [5] a) Q. Zhang, K. J. Takeuchi, E. S. Takeuchi, A. C. Marschilok, *Phys. Chem. Chem. Phys.* **2015**, 17, 22504; b) G. G. Amatucci, N. Pereira, *J. Fluorine Chem.* **2007**, 128, 243.
- [6] a) W. Liu, H. Li, J. Y. Xie, Z. W. Fu, *ACS Appl. Mater. Interfaces* **2014**, 6, 2209; b) Y. Shao, H. Yue, R. Qiao, J. Hu, G. Zhong, S. Wu, M. J. McDonald, Z. Gong, Z. Zhu, W. Yang, Y. Yang, *Chem. Mater.* **2016**, 28, 1026.
- [7] C. Jiang, B. J. Wang, Z. R. Wu, J. L. Qiu, Z. P. Ding, J. Zou, S. L. Chen, P. Gao, X. B. Niu, L. P. Wang, H. Li, *Nano Energy* **2020**, 70, 104552.
- [8] R. Yazami, *US 8377586*, **2013**.
- [9] G. Nagasubramanian, M. Rodriguez, *J. Power Sources* **2007**, 170, 179.
- [10] S. Long, F. Chen, F. Ding, Y. Han, X. Liu, Q. Xu, *J. Phys. Chem. C* **2019**, 123, 28048.
- [11] a) J. Read, E. Collins, B. Piekarski, S. Zhang, *J. Electrochem. Soc.* **2011**, 158, A504; b) M. A. Rodriguez, M. R. Keenan, G. Nagasubramanian, *J. Appl. Crystallogr.* **2007**, 40, 1097; c) G. Zhong, H. Chen, Y. Cheng, L. Meng, H. Liu, Z. Liu, G. Zheng, Y. Xiang, X. Liu, Q. Li, Q. Zhang, H. Yue, C. Lu, Y. Yang, *J. Mater. Chem. A* **2019**, 7, 19793; d) J. Wang, M. Sun, Y. Liu, J. Lin, L. Wang, Z. Xu, W. Wang, Z. Yuan, J. Liu, X. Bai, *J. Mater. Chem. A* **2020**, 8, 6105.
- [12] a) Y. Yuan, K. Amine, J. Lu, R. Shahbazian-Yassar, *Nat. Commun.* **2017**, 8, 15806; b) P. Gao, *Sci. Bull.* **2018**, 63, 1173.
- [13] A. Hamwi, *J. Phys. Chem. Solids* **1996**, 57, 677.
- [14] D. D. Chronopoulos, A. Bakandritsos, M. Pykal, R. Zboril, M. Otyepka, *Appl. Mater. Today* **2017**, 9, 60.
- [15] a) S. Kim, J. Cui, V. P. Dravid, K. He, *Adv. Mater.* **2019**, 31, 1904623; b) M. G. Boebinger, D. Yeh, M. Xu, B. C. Miles, B. Wang, M. Papakyriakou, J. A. Lewis, N. P. Kondekar, F. J. Q. Cortes, S. Hwang, X. Sang, D. Su, R. R. Unocic, S. Xia, T. Zhu, M. T. McDowell, *Joule* **2018**, 2, 1783.
- [16] P. Gao, L. Wang, Y. Y. Zhang, Y. Huang, L. Liao, P. Sutter, K. Liu, D. Yu, E. G. Wang, *Nano Lett.* **2016**, 16, 5582.
- [17] a) Y. Cheng, Z. Yao, Q. Zhang, J. Chen, W. Ye, S. Zhou, H. Liu, M. S. Wang, *Adv. Funct. Mater.*, <https://doi.org/10.1002/adfm.202005417>; b) Z. Yang, P. V. Ong, Y. He, L. Wang, M. E. Bowden, W. Xu, T. C. Droubay, C. Wang, P. V. Sushko, Y. Du, *Small* **2018**, 14, 1803108; c) F. Wang, H. C. Yu, M. H. Chen, L. Wu, N. Pereira, K. Thornton, A. Van der Ven, Y. Zhu, G. G. Amatucci, J. Graetz, *Nat. Commun.* **2012**, 3, 1201; d) Q. Li, Z. Yao, E. Lee, Y. Xu, M. M. Thackeray, C. Wolverton, V. P. Dravid, J. Wu, *Nat. Commun.* **2019**, 10, 1692; e) X. Wang, Z. Yao, S. Hwang, Y. Pan, H. Dong, M. Fu, N. Li, K. Sun, H. Gan, Y. Yao, A. Aspuru-Guzik, Q. Xu, D. Su, *ACS Nano* **2019**, 13, 9421; f) X. Wu, S. Li, B. Yang, C. Wang, *Electrochem. Energy Rev.* **2019**, 2, 467; g) X. H. Liu, J. Y. Huang, *Energy Environ. Sci.* **2011**, 4, 3844.
- [18] S. Chen, L. Wang, R. Shao, J. Zou, R. Cai, J. Lin, C. Zhu, J. Zhang, F. Xu, J. Cao, J. Feng, J. Qi, P. Gao, *Nano Energy* **2018**, 48, 560.
- [19] M. Sina, J. Alvarado, H. Shobukawa, C. Alexander, V. Manichev, L. Feldman, T. Gustafsson, K. J. Stevenson, Y. S. Meng, *Adv. Mater. Interfaces* **2016**, 3, 1600438.
- [20] E. Rangasamy, J. Li, G. Sahu, N. Dudney, C. Liang, *J. Am. Chem. Soc.* **2014**, 136, 6874.
- [21] G. Yoon, H. Kim, I. Park, K. Kang, *Adv. Energy Mater.* **2017**, 7, 1601519.
- [22] P. Boullay, L. Lutterotti, D. Chateigner, L. Sicard, *Acta Crystallogr. A Found. Adv.* **2014**, 70, 448.
- [23] F. Rao, Z. Wang, B. Xu, L. Chen, C. Ouyang, *Engineering* **2015**, 1, 243.
- [24] a) F. Wang, R. Robert, N. A. Chernova, N. Pereira, F. Omenya, F. Badway, X. Hua, M. Ruotolo, R. Zhang, L. Wu, V. Volkov, D. Su, B. Key, M. S. Whittingham, C. P. Grey, G. G. Amatucci, Y. Zhu, J. Graetz, *J. Am. Chem. Soc.* **2011**, 133, 18828; b) A. W. Xia, H. J. Lee, I. Capone, A. Robertson, T. U. Wi, J. Fawdon, S. Wheeler,

- H. W. Lee, N. Grobert, M. Pasta, *Nat. Mater.* **2020**, *19*, 644;
c) C. L. Li, K. Y. Chen, X. J. Zhou, J. C. Maier, *npj Comput. Mater.* **2018**,
4, 22; d) A. Kraysberg, Y. Ein-Eli, *J. Solid State Electrochem.* **2017**, *21*,
1907.
- [25] X. Fan, E. Hu, X. Ji, Y. Zhu, F. Han, S. Hwang, J. Liu, S. Bak, Z. Ma,
T. Gao, S. C. Liou, J. Bai, X. Q. Yang, Y. Mo, K. Xu, D. Su, C. Wang,
Nat. Commun. **2018**, *9*, 2324.
- [26] A. Lewandowski, P. Jakobczyk, *J. Solid State Electrochem.* **2016**, *20*,
3367.
- [27] a) G. Kresse, J. Hafner, *Phys. Rev. B: Condens. Matter.* **1993**, *47*, 558;
b) G. Kresse, J. Hafner, *Phys. Rev. B: Condens. Matter.* **1994**, *49*,
14251.
- [28] S. J. Clark, M. D. Segall, C. J. Pickard, P. J. Hasnip, M. I. J. Probert,
K. Refson, M. C. Payne, *Z. Kristallogr.* **2005**, *220*, 567.
- [29] J. P. Perdew, K. Burke, Ernzerhof, *Phys. Rev. Lett.* **1997**, *78*, 1396.
- [30] a) H. Graeme, P. U. Blas, J. Hannes, *J. Chem. Phys.* **2000**, *113*, 9901;
b) H. J. Graeme Henkelman, *J. Chem. Phys.* **2000**, *113*, 9978.
- [31] a) X. Zhang, C. Yang, Y. Pan, M. Weng, L. Xu, S. Liu, J. Yang, J. Yan,
J. Li, B. Shi, J. Yang, J. Zheng, F. Pan, J. Lu, *J. Mater. Chem. A* **2019**, *7*,
14042; b) C. Yang, X. Zhang, J. Ma, B. Shi, H. Zhang, L. Xu, J. Yang,
S. Liu, R. Quhe, F. Pan, J. Lu, D. Yu, *J. Electrochem. Soc.* **2020**, *167*,
020538; c) C. Yang, X. Zhang, J. Li, J. Ma, L. Xu, J. Yang, S. Liu,
S. Fang, Y. Li, X. Sun, X. Yang, F. Pan, J. Lu, D. Yu, *Electrochim. Acta*
2020, *346*, 136244.